New Journal of Physics
The open-access journal for physics

Chemical sputtering of carbon films by simultaneous irradiation with argon ions and molecular oxygen

C Hopf[1], **M Schlüter, T Schwarz-Selinger, U von Toussaint and W Jacob**

Max-Planck-Institut für Plasmaphysik, EURATOM Association, Boltzmannstrasse 2, 85748 Garching, Germany
E-mail: Christian.Hopf@ipp.mpg.de

New Journal of Physics **10** (2008) 093022 (27pp)
Received 21 May 2008
Published 23 September 2008
Online at http://www.njp.org/
doi:10.1088/1367-2630/10/9/093022

Abstract. The erosion of hard amorphous hydrocarbon films by bombardment with argon ions and simultaneous exposure to thermal molecular oxygen is studied as a function of oxygen flux density (0–11 400 times the ion flux density), ion energy (20–800 eV), and surface temperature (110–875 K). While erosion due to Ar^+ ions only is dominated by physical sputtering, the additional presence of molecular oxygen leads to a marked increase of erosion, indicating chemical sputtering. The erosion yield increases with both ion energy and oxygen flux density. Starting from about 700 K thermal chemical erosion (combustion) by O_2 is observed even without ion bombardment. Additional ion bombardment in this temperature range causes an increase of the erosion rate over the sum of thermal chemical erosion and the rate observed at room temperature. Below ≈300 K, the rate increases with decreasing temperature. We explain the latter behavior by the ion-induced reaction of adsorbed oxygen which constitutes a significant surface coverage only at low temperatures. A rate equation model is presented, which incorporates the mechanisms of physical sputtering, chemical reaction of O_2 at reactive sites created by ion bombardment, the ion-induced reaction of adsorbed oxygen and ion-enhanced thermal chemical erosion. The model's nine free parameters are optimized by fitting 68 experimental data points. The model yields good agreement in all investigated dependences.

[1] Author to whom any correspondence should be addressed.

Contents

1. Introduction

Oxygen plasmas are commonly used to etch carbon-based thin films or remove carbon impurities from surfaces. For example, they are applied for patterning or photoresist-removal processes in microelectronics fabrication [1]–[6], for the removal of diffusion-barrier carbon coatings on PET bottles prior to recycling [7], for the cleaning of optical components in synchrotron beamlines [8] and for plasma sterilization [9]–[12].

In nuclear-fusion research, carbon first-wall components are eroded due to hydrogen species from the plasma and the resulting hydrocarbons are redeposited in other locations [13]–[15]. In a future deuterium/tritium fusion experiment, such as the future international thermonuclear experimental reactor (ITER), this erosion–redeposition cycle will lead to a monotonically increasing tritium inventory, which may soon exceed safety limits. Among others [16], combustion of the redeposited hydrocarbon films in an oxygen atmosphere as well as their erosion in oxygen glow discharges are considered as candidate techniques for regular tritium removal [16]–[21]. In both cases, the erosion products are the volatile oxides CO, CO_2 and H_2O, and, besides, H_2 [1, 22, 23].

Combustion of carbon with molecular oxygen is surely among the most important chemical reactions in both nature and civilization. It has been extensively studied in the literature (for reviews see [22, 24]). The reactivity toward oxygen molecules strongly depends on the nature of the carbon material [22, 25, 26]. For hard amorphous hydrogenated carbon (a-C:H) films thermal chemical erosion (combustion) sets in around 650 K [27].

In an oxygen plasma additional species are created besides O_2, namely neutral atomic oxygen and ozone as well as atomic and molecular oxygen ions. Thermal oxygen atoms exhibit a much higher reactivity with carbon than O_2 at moderately elevated temperatures [28]. Ozone

is known to react at room temperature with graphite and carbon black and produce carbon oxides [29]. The ions, on the other hand, are accelerated in the plasma sheath to energies between a few electron-volts and several hundred electron-volts, depending on the method of plasma generation. These energetic oxygen species cause erosion rates which exceed those of physical sputtering due to chemical reactions at the end of their range, a phenomenon known as chemical sputtering or reactive ion etching [30]–[33].

On a carbon surface in direct contact with an oxygen plasma all the mentioned species impinge simultaneously. Given the experience with other plasma–wall-interaction systems, it may be suspected that there exist synergisms or anti-synergisms between the different incident species. For example, a drastic enhancement of the erosion of silicon due to XeF_2 was found in the presence of argon ion bombardment [34], and a similar observation was made for the erosion of graphite and a-C:H by atomic hydrogen in the presence of argon ion bombardment [35]–[37].

Indeed, it has been shown in the literature that synergisms play an important role also in oxygen plasma erosion of carbon films. For a-C:H, Jacob *et al* [18] and Landkammer *et al* [38] found that the erosion rate increases with both ion energy and temperature. These two dependences indicate that ballistic as well as chemical processes play a role. Baggerman *et al* [39] reported measured yields for polymer etching in oxygen plasmas of up to ≈ 14 removed carbon atoms per incident energetic oxygen particle. This yield is by about a factor of six higher than in a similar Ar discharge. By means of a heat balance they were able to show that exothermic reactions occur at the surface. From this latter finding they concluded that the oxidation reactions take place at the surface and that, therefore, the yields can only be explained if neutral oxygen species contribute to the erosion process at the surface. The same conclusion was reached by Gokan and Esho [40]. When bombarding polymer films with oxygen ions in an oxygen atmosphere, they measured yields >2. As their main ion species was O_2^+ and their main carbon-carrying erosion products were CO and CO_2, they postulated that there must be a synergism between the ions and neutral oxygen species to explain the high yields.

The ratio of the fluxes of neutral oxygen species and ions can be changed in discharges with mixtures of noble gas and oxygen as source gas. Pure noble gas discharges only cause physical sputtering with low rates if the ion energy is kept small. When oxygen is admixed to the discharge a steep increase of the rates was observed by Murillo *et al* [41] for polymer (hexatriacontane) etching in Ar plasmas and by Hopf *et al* [42] for a-C:H etching in He plasmas. In the experiments of Hopf *et al*, the erosion rate already saturated at an $O_2/(O_2 + He)$ ratio of $\approx 10\,\%$. It was concluded that below this oxygen concentration the rate is limited by the supply of neutral oxygen species, and above this concentration by the ion flux.

Under conditions of sufficient oxygen supply, i.e., when the rate is limited by the ion flux rather than the oxygen flux, Baggermann *et al* [39] as well as Landkammer [23] showed that the erosion rate depends linearly on the energy flux density of energetic particles onto the surface. By eroding a-C:H in discharges of mixtures of oxygen and noble gases with varying mixture ratio, Landkammer [23] could even show that this linear dependence holds independent of whether the energy flux density is mainly carried by noble gas or oxygen ions. This finding again suggests that the chemical reactivity is mainly supplied by neutral oxygen species.

There is a widespread belief in the literature that atomic oxygen is the most important neutral species in typical technical oxygen plasma applications for carbon etching [41, 43]. Indeed, experiments confirm a high reactivity of the reactive neutral oxygen species even at room temperature. By exposing narrow gaps with a-C:H-coated side walls and bottoms and a depth-to-width ratio below five to the afterglow of an ECR oxygen plasma Schwarz-Selinger

et al [44] could show that more than 90% of O and O_3 were lost on the way to the bottom of the gap. However, despite their obviously high surface loss probabilities these species seem to be not very important for the ion–neutral synergism in the plasma. Collart *et al* [45] showed that their fluxes of atomic oxygen, measured by laser-induced fluorescence, are by far not sufficient to explain their observed erosion rates of polymers exposed to an oxygen plasma even when assuming an erosion probability of 1 C/O. Hence, it was concluded that molecular oxygen is the most important chemically reactive species in the investigated plasma.

Indeed, the observation of synergistic erosion of graphite by an argon ion beam and O_2 gas was reported by Vietzke *et al* [46] in 1987. Even at room temperature, where thermal oxygen molecules do not gasify carbon, the combined bombardment leads to strong erosion. We have recently investigated the synergism in more detail for a-C:H as target material [47]. For 400 eV Ar^+ bombardment, we demonstrated that the erosion rate shows a pronounced increase when offering an increasing flux of thermal molecular oxygen. At oxygen/ion flux ratios in excess of 10 000 erosion yields of more than 4 carbon atoms per incident ion were measured.

Both etching with suitable reactive ions and synergistic erosion due to combined exposure to suitable reactive thermal neutrals and ions, which may be either inert or reactive as well, are commonly referred to as chemical sputtering [33]. Nevertheless, the use of this term in the literature is not very consistent. To avoid confusion, we define chemical sputtering as a process in which ion bombardment induces chemical reactions which finally lead to the formation of volatile erosion products. While Jacob and Roth [33] point out that the erosion products' 'release will mostly be thermally driven', recent molecular dynamics simulations of Ar^+/H cobombardment of a-C:H [48] indicate that the final desorption of the erosion products happens through ion-induced breaking of the last bond with the film. Chemical sputtering is distinctly different from thermal chemical erosion of carbon in oxygen at high temperatures on the one hand, where bond-breaking due to energetic atoms is not required, and from physical sputtering on the other hand, where chemical bonds are broken due to momentum transfer but the formation of new chemical bonds plays no role. The terms *erosion rate* and *erosion yield* are used in this paper as generic terms without specifying which mechanism is responsible for the observed erosion.

In the present paper, we present an extended parameter study of the synergistic erosion of a-C:H due to combined Ar^+ and O_2 exposure. Furthermore, based on a microscopic picture of the underlying processes, we develop an integrated rate equation model which describes the erosion rate as a function of all experimentally varied parameters, the particle flux densities, the surface temperature and the ion energy.

2. Experimental

The experiments are performed in the UHV particle beam setup MAJESTIX. Only a short description of the parts relevant for this work shall be given here. More details can be found in [49].

The samples we study are hard a-C:H films deposited on silicon wafers. The advantage of these films on a reflective substrate is that, as opposed to other carbon-based materials, they are well suited for ellipsometry due to their high transparency. The films are deposited by means of a capacitively coupled radio-frequency (RF) discharge in methane inside the setup's combined preparation chamber and load lock. In order to allow transfer of the sample between the experiment chamber and the preparation chamber the wafer is mounted in a metal frame. For

deposition, the frame with the silicon wafer is slid into an electrically well contacted position on a sample stage. The stage is connected capacitively to a 13.6 MHz RF supply and electrically insulated from the grounded chamber walls. The films are hard a-C:H with a refractive index of $n = 2.20 - i0.14$, an H/(H+C) ratio of approximately 0.3 and a carbon number density of $\approx 1 \times 10^{23}$ cm^{-3} [50]. Typically, the film is deposited to a thickness of ≈70 nm.

Transfer of the sample between the preparation and the target chamber takes place *in vacuo*. The sample with its stainless steel frame is positioned in the sample holder. The sample can be heated by a filament in the holder behind the sample. The design of the sample holder is symmetrical with respect to the filament with a second silicon wafer opposite to the sample. This allows the sample temperature in heating mode to be measured with a thermocouple glued to this second wafer. Temperatures up to ≈900 K can be reached.

Alternatively, the sample holder can be cooled with cold nitrogen gas. In this case, the temperature is held constant by simultaneous controlled heating of the sample. Temperatures down to 110 K can be reached. As good thermal contact between the silicon substrate and the sample holder is required, the metal frame in this case is made of copper and contacts the whole back side of the sample. With this substrate frame the symmetry of the sample holder with respect to the heat source or sink is no longer fulfilled. Therefore, in cooling mode the temperature is measured with a thermocouple pressed to the sample's front surface close to the measurement spot.

The interacting particles in this work are ions, generated in a low-energy ion gun, mass selected in a Wien filter and focused onto the sample, and oxygen molecules, which are admitted through a variable leak into the chamber. The ion current density is determined by a Faraday cup with an entrance aperture of 1.5 mm diameter, which can be moved into the sample position. The flux density of oxygen is calculated from the oxygen partial pressure and the wall temperature of 300 K, which is also assumed to be the gas temperature. The O_2 pressure, which is in the range between 4×10^{-8} and 2×10^{-4} mbar, is measured with an ionization gauge which was calibrated for O_2 by comparison with a spinning rotor gauge at higher pressures. The O_2 pressure is measured before the ion gun is switched on, as argon from the ion gun leads to a non-negligible increase of the chamber pressure. By monitoring the residual gas, which is dominated by H_2, with a quadrupole mass spectrometer it is ensured that all other partial pressures are small compared with that of O_2 and, especially, that the water pressure is below 10^{-10} mbar and thus low enough not to cause enhanced erosion at the lowest temperatures [51].

Ellipsometry at a fixed wavelength of 632.8 nm is employed as a very sensitive technique to detect thickness changes of the films with sub-monolayer resolution and thus determine erosion rates of less than 10^{10} C atoms cm^{-2} s^{-1} ≈ 10^{-6} nm s^{-1} *in situ* and in real time. The ellipsometry laser is reflected in the ion beam's interaction spot on the sample.

Ellipsometry is evaluated by comparison of the time-dependent measured ellipsometric angles, $\Psi(t)$ and $\Delta(t)$, with those calculated from an optical model of the film, i.e. a depth and time-dependent complex refractive index $n(x, t)$, where x is the depth below the film surface and $d = \max(x)$ is the film thickness. As $\Psi(t)$ and $\Delta(t)$ do not uniquely define $n(x, t)$, assumptions about $n(x, t)$ must be made. Firstly, a freshly deposited film is known to be homogeneous and therefore has a constant refractive index independent of depth. During ion bombardment the film is modified only to a maximum ion penetration range, x_{mod}. We can therefore assume $n(x) = n_{\mathrm{bulk}}$ for $x > x_{\mathrm{mod}}$. For $0 < x < x_{\mathrm{mod}}$, the film is being modified and at the same time eroded. If $x_{\mathrm{mod}} < d$, a steady state will finally be reached in which $\partial n(x, t)/\partial t = 0$. In this case, the only time-dependent parameter in the model is the thickness of the bulk layer,

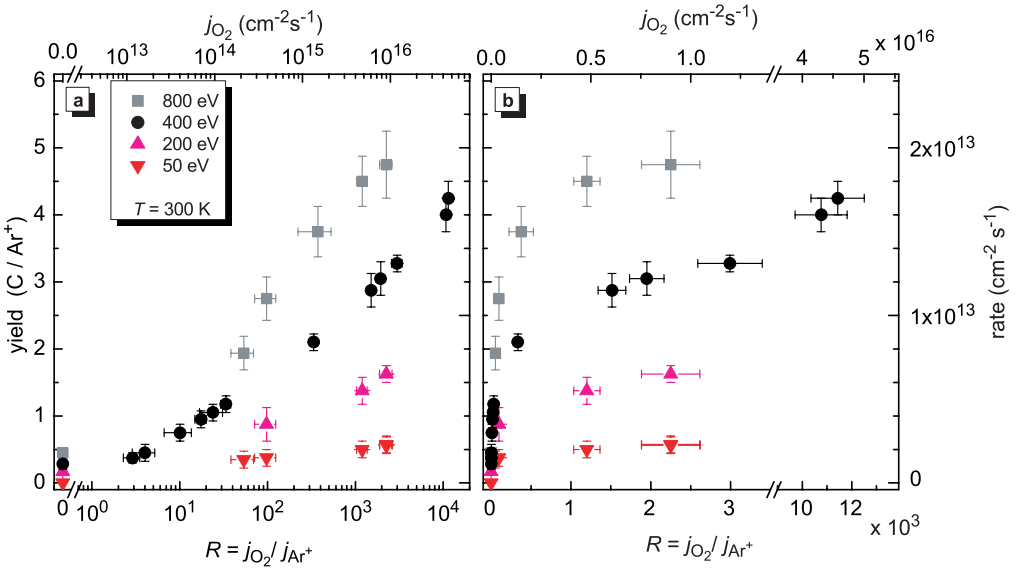

Figure 1. Erosion rate (right ordinate) and yield (left ordinate, eroded C per incident Ar^+) as a function of the oxygen flux density (top abscissae) for combined exposure of a-C:H to Ar^+ ions and O_2 molecules at 300 K, constant ion flux density of 4×10^{12} cm^{-2} s^{-1} and different ion energies. The bottom abscissae give the ratio R of the oxygen and ion flux densities. (a) Shows the data on a logarithmic abscissa on the right-hand side of the axis break and (b) shows a linear representation.

$d_{\text{bulk}}(t) = d(t) - x_{\text{mod}}$. It is usually sufficient to describe the modified top layer with a constant refractive index $n(0 < x < x_{\text{mod}}) = n_{\text{mod}}$.

In the case of exposure to oxygen at high temperatures the described assumptions break down as modification of the films is not only induced by the ions but also by thermal oxygen and affects the whole film. The maximum temperature up to which the assumption of an unmodified bulk is justified was derived in a separate experiment. In a first step, several films were eroded to approximately half thickness by exposure to O_2 at various temperatures. In a second step, the remnants of the films were eroded at room temperature in an oxygen ECR plasma and monitored with ellipsometry. It is known that under these conditions with a low sheath potential of the order of 5 eV the films are eroded almost layer by layer without modification. Thus the thickness of the modified layer from the experiment at high temperature can be determined. It was found that significant film modification due to exposure to O_2 only starts above ≈850 K.

3. Results

Figure 1 shows the erosion yield as a function of the flux ratio $R = j_{O_2}/j_{\text{ion}}$ on a logarithmic (a) and a linear (b) abscissa. Unless otherwise stated, all yields in this paper are the rate of erosion of carbon atoms Γ normalized to the incident ion flux density j_{ion}, $Y = \Gamma/j_{\text{ion}}$, where Γ and j_{ion} both have units of atoms per unit area and time interval. In all experiments with the ion beam switched on, the ion flux density was kept constant at $j_{\text{ion}} = 4 \times 10^{12}$ cm^{-2} s^{-1}, and only the O_2 flux density j_{O_2} was varied. Therefore, the erosion rate differs from the yield only by a constant factor and we can show it as an alternative ordinate on the right-hand side. We use this double

ordinate in all graphs in this paper, as it allows us to also show data of experiments without ion bombardment, where due to $j_{\mathrm{ion}} = 0$ no yields can be calculated.

The flux dependence in figure 1 is shown at four different ion energies of 50, 200, 400 and 800 eV. The sample temperature is 300 K, a temperature at which no erosion due to exposure to O_2 alone can be observed; the films can be stored in air over years without any detectable decrease of thickness. Without oxygen flux, shown on the left side of the axis break, the steady state erosion rates are governed by physical sputtering with yields below the detection limit at 50 eV and up to 0.45 at 800 eV. When there is a background pressure of molecular oxygen in the chamber the yields start to increase; in the case of 50 eV ions the yield is already 0.35 when the oxygen flux density is 50 times that of the ions. At $R \approx 2000$ the yields at the investigated energies between 200 and 800 eV are about ten times those of the physical sputtering yields. The highest recorded yield is that at 800 eV and $R = 2250$ with a value of 4.75. For comparison, the maximum physical sputtering yield of hard a-C:H under Ar^+ bombardment is $\approx$1.2 at 15 keV, as predicted by TRIM.SP [52] simulations using the parameters given in section 5.4. The linear representation in figure 1(b) shows that the rise of the yield slows down at higher flux ratios, indicating that the ion flux density starts to limit the rate.

The 400 eV data in figure 1 are those presented earlier in [47]. However, there are—erroneously—some additional data points in figure 1 of Hopf *et al* [47]. These correspond to measurements aimed at calibrating the oxygen flux density for a different gas inlet via comparison with the rates measured during chemical sputtering at 400 eV and room temperature. Thus for these data points only the rate is a measured value, whereas the oxygen flux density was determined such that they lie on a fit through the other data points, for which j_{O_2} was known.

The observed enhancement of the erosion yields over physical sputtering in the presence of molecular oxygen is an indication of chemical sputtering. It reminds of the chemical sputtering by thermal atomic hydrogen and ion bombardment mentioned in the introduction. The notable difference is that *molecular* oxygen shows this synergistic erosion whereas in the hydrogen case atomic species are required. In the hydrogen case, it was found that the yield depends on the ion energy, or more explicitly it scales like the damage produced in a near surface region [37, 53]. If a similar process is underlying the synergism with oxygen molecules, we would expect to find a similar increase of the erosion rate with energy in this case.

The dependence of the erosion rate/yield on ion energy in the range 20–800 eV is shown in figure 2 at three different temperatures of 150, 300 and 800 K. Additionally, the erosion rate at 800 K due to the same flux density of oxygen but without ion bombardment is shown as dashed line, as it poses a lower limit for Ar^+/O_2 at 800 K. For both 150 and 300 K, there is a factor of $\approx$30 increase of the yield between 20 and 800 eV. The two data points at 800 K also show a comparable slope. The yields at 800 K are higher than those at 300 K due to the additional effect of thermal chemical erosion. Interestingly, the yields at 150 K also lie above those at room temperature.

The complete set of measured temperature-dependent yields/rates is shown in figure 3 for the case of combined exposure to Ar^+ and O_2 at ion energies between 20 and 800 eV and, additionally, without ion bombardment (open circles). In the latter case, we detect thermal chemical erosion by O_2 from 700 K onwards. The energy dependences of figure 2 are vertical sections in figure 3 at the corresponding temperatures. The flux densities were constant at $j_{\mathrm{ion}} = 4 \times 10^{12}\,\mathrm{cm^{-2}\,s^{-1}}$ and $j_{O_2} = 9 \times 10^{15}\,\mathrm{cm^{-2}\,s^{-1}}$.

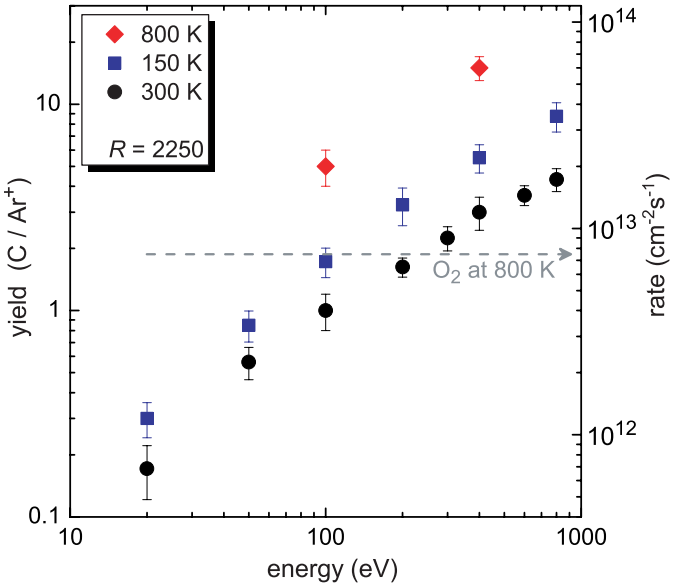

Figure 2. Erosion yield and rate of a-C:H due to combined exposure to Ar^+ ions and O_2 molecules as a function of ion energy at three different target temperatures. The flux densities are constant at $j_{ion} = 4 \times 10^{12}\,cm^{-2}\,s^{-1}$ and $j_{O_2} = 9 \times 10^{15}\,cm^{-2}\,s^{-1}$. The dashed horizontal arrow shows the chemical erosion rate measured at 800 K without ion bombardment.

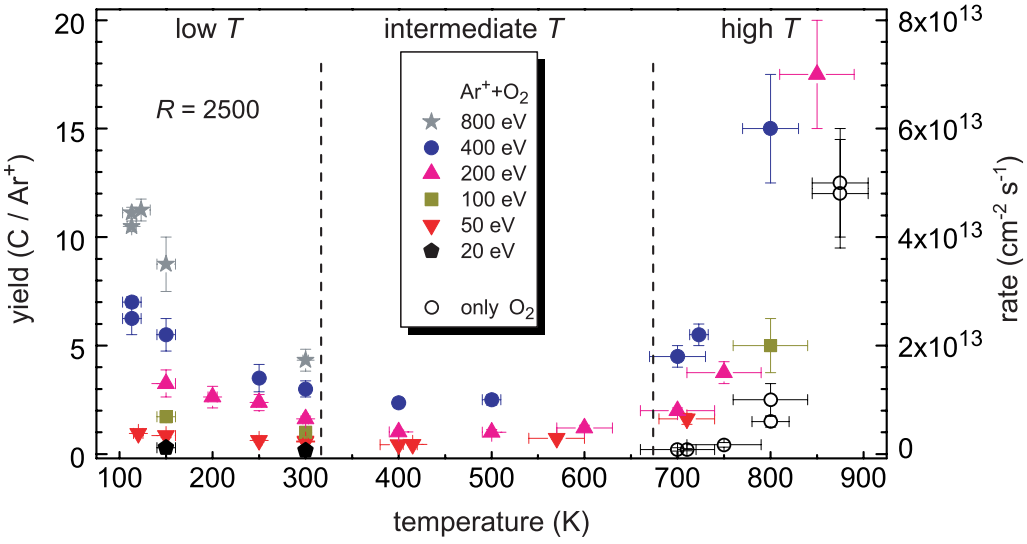

Figure 3. Erosion yield and rate of a-C:H due to combined exposure to Ar^+ ions and O_2 molecules as a function of target temperature at different ion energies. The open circles show the thermal chemical erosion rate without ion bombardment. The flux densities are $j_{ion} = 4 \times 10^{12}\,cm^{-2}\,s^{-1}$ and $j_{O_2} = 9 \times 10^{15}\,cm^{-2}\,s^{-1}$.

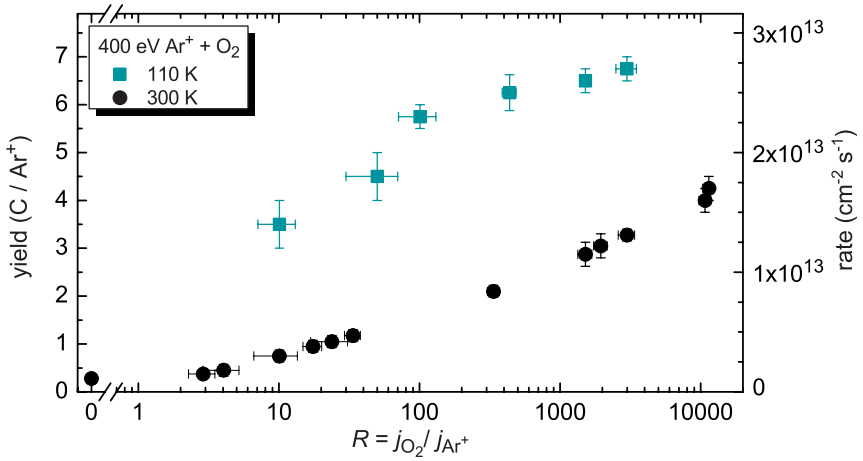

Figure 4. Erosion yield and rate as a function of the oxygen-to-ion flux ratio for combined exposure of a-C:H to Ar^+ ions and O_2 molecules at 400 eV ion energy and two different target temperatures of 300 and 110 K. The ion flux density is constant at 4×10^{12} cm^{-2} s^{-1}.

Figure 4 shows again the flux dependence data at 400 eV and 300 K already shown in figure 1 and compares them to rates measured for the same energy at 110 K. Again a higher rate is seen in the whole range of R. The 110 K data show a much faster rise at low R and appear to reach saturation earlier than at 300 K.

4. Discussion of the results

We find three rather distinct temperature ranges in figure 3: (i) in the case with only O_2 molecules thermal chemical erosion (CE) is detected starting from 700 K—from here onwards referred to as the *high temperature range*—with a fast increase with temperature. Simultaneous ion bombardment in this temperature range leads to an additional enhancement, which increases with ion energy. (ii) At *intermediate temperatures*, $300\,\mathrm{K} \lesssim T \lesssim 700\,\mathrm{K}$, a clear enhancement of erosion with respect to physical sputtering (PS) is observed, as already seen in the 300 K results in figures 1 and 2. In this temperature range, the rate is almost constant. (iii) In the *low temperature range*, $T \lesssim 300\,\mathrm{K}$, the rates increase again down to the lowest investigated temperature of 110 K. In the next paragraphs, we will discuss the three distinct temperature ranges one after the other.

In the intermediate temperature range, erosion is not observed without ion bombardment. Furthermore, no sputtering is observed for bombardment by ions only, if the ion energy is below the threshold for PS, as is the case at 20 and 50 eV energy in the experiment. Thus, the mechanism observed is of purely synergistic nature. It is plausible to assume that the thermal oxygen species partake in the erosion process by means of their chemical reactivity. As the rates show no temperature dependence in the range 400–600 K it may be speculated that the process active in this temperature range is indeed independent of temperature as it involves no thermally activated reaction steps. This might possibly happen via the creation of sufficiently long-lived reactive sites by ion bombardment at which incoming O_2 can react without having to overcome an activation barrier. Gokan and Esho [40] proposed such a mechanism and developed a model

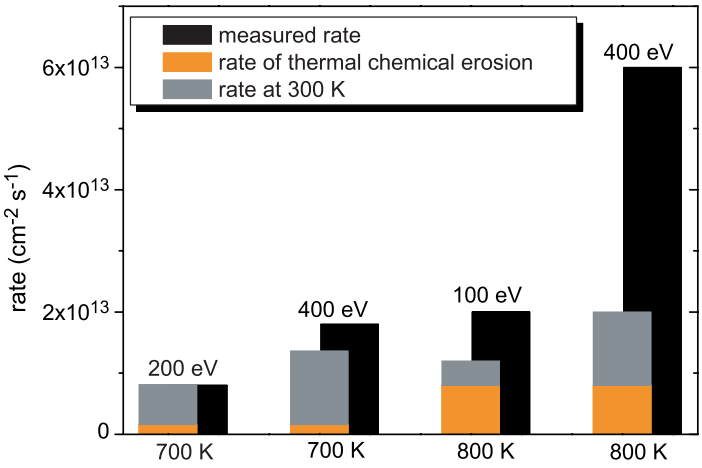

Figure 5. Comparison of the sum of the rates of CE and CS at 300 K with the measured erosion rate for combined Ar^+/O_2 exposure for various experimental conditions as given in the graph. The orange bar shows the CE rate at the indicated temperature due to oxygen exposure only, the gray bar shows the CS rate at 300 K due to combined exposure to O_2 and Ar^+ at the indicated ion energy, and the black bar gives the erosion rate measured at the indicated temperature and energy for combined exposure. The flux densities are $j_{ion} = 4 \times 10^{12}\,cm^{-2}\,s^{-1}$ and $j_{O_2} = 9 \times 10^{15}\,cm^{-2}\,s^{-1}$.

to describe the dependence of the erosion rate on the ion-to-neutral flux ratio. We will refer to this process simply as *chemical sputtering* (CS).

In the high temperature range, ion bombardment is found to increase the total erosion rates over the CE rates. The most simple assumption would be that in this temperature range the CS rate observed at around 300 K adds to CE with no mutual influence of the two processes on each other. Figure 5 compares the rates observed at 700 and 800 K with the sum of the corresponding CE rate and the CS rate at 300 K. In all cases except 700 K/200 eV the observed rate is clearly higher than this sum. This indicates that, besides these two mechanisms, a third, new mechanism must be active. We interpret this additional contribution as an enhancement of CE caused by ion bombardment. Such an interpretation was earlier given by Roth and García-Rosales [54] who observed a similar enhancement in the case of hydrogen ion bombardment of graphite at elevated temperatures. In their analytic description of the total erosion yield Roth and García-Rosales included this enhancement for energetic hydrogen ions by multiplying the erosion yield of thermal H atoms with a factor $(1 + D_{Roth} Y_{phys})$, where D_{Roth} is the enhancement constant and the physical sputtering yield Y_{phys} is used to estimate the yield of creation of reactive sites. Schlüter *et al* [55] have recently confirmed the enhancement of CE due to ion bombardment for exposure of a-C:H to Ar ions and atomic hydrogen at higher temperatures. In the remainder of the paper, we refer to this mechanism as *ion-enhanced chemical erosion* (IECE).

The most notable feature in figure 3 is that the erosion rate also increases when decreasing the temperature below room temperature; at 400 and 800 eV the yields at 110 K are roughly twice those at 300 K. In [47], we have already explained this effect as the ion-induced reaction of adsorbed oxygen with the atoms of the film. The products of these reactions are volatile carbon oxides and water. As the adsorbed oxygen is weakly bound to the surface, thermal desorption competes with adsorption and a temperature-dependent steady-state surface coverage

with oxygen is established. As temperature rises, desorption increases and, hence, the surface coverage drops. In the most simple case the rate of the ion-induced reaction will be proportional to the oxygen surface coverage and, therefore, will also decrease with increasing temperature.

The principle occurrence of this type of ion-induced reaction in an adsorbed layer was proven in various systems. In the chemical sputtering of silicon with noble gas ions and fluorine species a similar increase of the erosion rate with decreasing temperature was found [56, 57]. However, as opposed to our case, the chemically reactive precursor, either F atoms or XeF_2, leads to spontaneous etching (without ion bombardment) even below room temperature. This spontaneous etch rate decreases in the temperature range from 300 to 77 K [56] for F atoms and increases in the case of XeF_2. The temperature dependence below approx. 300 K for both chemical sputtering with Ar^+/XeF_2 and spontaneous etching with XeF_2 was explained in terms of a temperature-dependent steady state physisorbed XeF_2 coverage [58, 59]; increasing temperature leads to an increasing desorption rate of XeF_2 which is bound to the surface with $\approx$0.03 eV. The rate of the ion-induced chemical sputtering reaction is proportional to the XeF_2 coverage and hence decreases with increasing temperature.

For a case similar to the one described in this paper—the simultaneous exposure of a-C:H to Ar^+ ions and water—a very similar increase of the erosion rate toward lower T was seen [51]. In this case, the formation of an adsorbed layer can be directly deduced as, when increasing the water pressure and/or switching off the ion beam, the continuing growth of an ice layer can be observed by ellipsometry. The observation of enhanced erosion at temperatures at which ice growth is possible, but at water-to-ion flux ratios where a steady-state surface coverage with water is established, shows that in principle this kind of ion-induced reaction between adsorbed oxygen and carbon is possible. According to the definition given in the introduction, this process also has to be considered as chemical sputtering. In order to distinguish the two different mechanisms of chemical sputtering, we refer to this one as *adsorbed layer chemical sputtering* (ALACS).

Joubert *et al* [60], Vanderlinde and Ruoff [61], and Standaert *et al* [62] have also proposed the ion-induced reaction of adsorbed oxygen as the mechanism of the synergism between ion bombardment and O_2 and have successfully modeled flux dependences based on this mechanism. However, the only mechanism of desorption of oxygen in all of these models is ion-induced desorption, either by physical sputtering of unreacted O atoms [61] or by the ion-induced erosion reaction itself [60]–[62]. All these models do not take the thermal desorption of O_2 into account, which we assume to be responsible for the temperature dependence observed in our experiments at low T. The thermal desorption, however, leads to a negligible oxygen coverage and a vanishing rate of the ALACS mechanism in the intermediate temperature range, in contrast to the rather constant measured rate. Hence, there needs to be an additional mechanism of chemical sputtering which can either be the CS mechanism described above or alternatively an ALACS mechanism which acts on a second, more strongly bound adsorbed oxygen population that does not thermally desorb in the intermediate T range. In the model presented in the following section we choose the CS mechanism.

5. Modeling

In the previous section the observed dependences were explained by a number of different erosion mechanisms. In this section, a rate equation model is developed which incorporates all these mechanisms. The mechanisms fall into two groups, the individual actions of the two

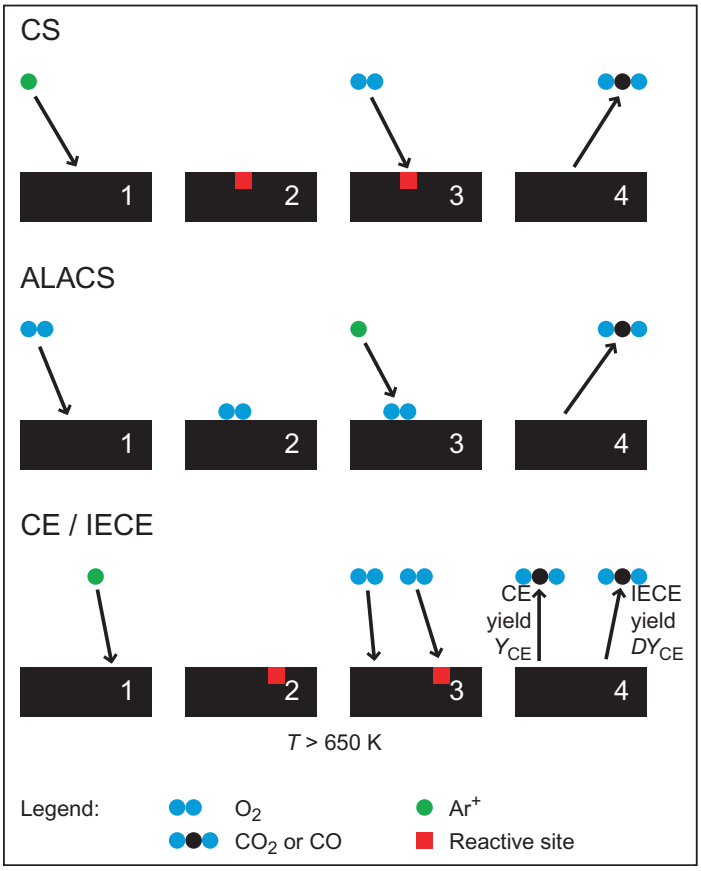

Figure 6. Schematic of the synergistic erosion mechanisms. CS: an energetic ion creates a reactive site. Incoming O_2 reacts at this site and forms a volatile carbon oxide. ALACS: at first oxygen adsorbs at the surface. An incoming energetic ion hits the adsorbed oxygen leading to the production of a volatile carbon oxide. CE and IECE: at temperatures in excess of about 650 K O_2 can directly react at the surface and form a volatile oxide with a yield Y_{CE}. On a reactive site which was created by prior ion bombardment the CE yield is enhanced by a factor D.

particle fluxes and synergistic interactions, for which both particle fluxes are required. The individual actions are

(i) physical sputtering (PS) due to ion bombardment and
(ii) (thermal) chemical erosion (CE) by molecular oxygen at elevated temperatures.

The synergistic interactions are

(iii) chemical sputtering (CS), in which incident O_2 reacts at already present, sufficiently long-lived reactive sites created by ion bombardment,
(iv) adsorbed-layer chemical sputtering (ALACS), in which ion bombardment induces reactions between already adsorbed oxygen and the film's atoms, and
(v) ion-enhanced chemical erosion (IECE), where ion bombardment enhances the reactivity of the surface toward O_2 at elevated temperatures.

The mechanisms CS, ALACS, CE and IECE are schematically depicted in figure 6.

In the following, we assume that our surface has a fixed areal density of sites, n_0, and that each such site belongs to exactly one of a set of populations. The fraction of sites that belongs to a population i is given by the corresponding surface coverage Θ_i with $\sum_i \Theta_i = 1$. We do not explicitly account for the hydrogen in the film, but assume, for simplicity, that it will be eroded along with the carbon according to the film's stoichiometry. In this sense, n_0 can be regarded as the undisturbed film's surface carbon density which is typically $10^{15}\,\mathrm{cm}^{-2}$. In order to describe all the mechanisms listed above, we have to at least consider three surface coverages: undisturbed carbon sites (Θ_C), reactive sites (Θ_r), and sites where oxygen is adsorbed (Θ_O). For the creation of the latter sites, again for simplicity, we only consider dissociative adsorption by which finally two sites will have one O atom adsorbed.

5.1. Contributions to the erosion rate

The erosion rate can be written as the sum of the rates of the five mechanisms listed above,

$$\Gamma = \Gamma_\mathrm{PS} + \Gamma_\mathrm{CE} + \Gamma_\mathrm{CS} + \Gamma_\mathrm{ALACS} + \Gamma_\mathrm{IECE}. \tag{1}$$

Each individual rate is given by the product of one of the particle fluxes, j_k, the surface coverage of the population on which the mechanism can happen, Θ_i, and a corresponding yield Y_l or probability p_l. Maintaining the order of the terms as in (1) we obtain

$$\Gamma = j_\mathrm{ion} Y_\mathrm{PS} + j_{\mathrm{O}_2} Y_\mathrm{CE} + j_{\mathrm{O}_2} p_\mathrm{CS} \Theta_\mathrm{r} + j_\mathrm{ion} Y_\mathrm{ALACS} \Theta_\mathrm{O} + j_{\mathrm{O}_2} Y_\mathrm{CE} D \Theta_\mathrm{r}, \tag{2}$$

where the factor D in the last term is a constant factor by which CE is enhanced on a reactive site. With this ansatz, we follow the treatment of Roth and García-Rosales [54] in close analogy (see section 4). As PS and CE are assumed to take place on all populations there appear no surface coverages in the corresponding terms.

Combining the terms which describe CE and IECE, we finally get

$$\Gamma = j_\mathrm{ion} Y_\mathrm{PS} + j_{\mathrm{O}_2} p_\mathrm{CS} \Theta_\mathrm{r} + j_\mathrm{ion} Y_\mathrm{ALACS} \Theta_\mathrm{O} + j_{\mathrm{O}_2} Y_\mathrm{CE} (1 + D\Theta_\mathrm{r}). \tag{3}$$

The yield given in the graphs is this rate normalized to the ion flux density,

$$Y = \Gamma / j_\mathrm{ion}. \tag{4}$$

5.2. Balance of surface coverages

The surface coverages in (3) are the steady-state result of rate equations which describe processes that change the population to which a site belongs. The processes and their rates are summarized in table 1. We assume the following processes: oxygen can adsorb at either undisturbed carbon or reactive sites with two different probabilities p_ad^C and p_ad^r (a). Reactive sites are created by ion impact on an undisturbed carbon site (b). An oxygen-covered site can become an undisturbed carbon site by thermal desorption of oxygen (c). The remaining processes are three of the aforementioned erosion mechanisms, ALACS which occurs at O-covered sites and leaves behind an undisturbed site (d), and CS (e) and IECE (f) which both transform a reactive into an undisturbed site.

Two of these terms in table 1 need further explanation. The factor B in process (b), the creation of reactive sites, leads to a limitation of the maximum value of Θ_r. Indication has been found earlier that the maximum coverage by reactive sites—usually associated with dangling bonds—is limited to about 10% by recombination of neighboring dangling bonds [63]. By introducing the factor B, we follow the mathematical treatment in [63]. The value given there,

Table 1. Schematic of the processes assumed in the model. The arrows on the right side show which coverage the processes convert into which other coverage. The terms in the middle column give the rates of the processes.

Process	Rate	Θ_C	Θ_O	Θ_r
(a) O_2 adsorption	$j_{O_2} p^C_{ad} \Theta_C$, $j_{O_2} p^r_{ad} \Theta_r$	→	←	
(b) Creation of reactive sites	$j_{ion} Y_r (1 - \Theta_O - B\Theta_r)$			→
(c) O_2 desorption	$A\Theta_O$		←	
(d) ALACS	$j_{ion} Y_{ALACS} \Theta_O$		←	
(e) CS	$j_{O_2} p_{CS} \Theta_r$			←
(f) IECE	$j_{O_2} Y_{CE} D \Theta_r$			←

$B = 13$, gave reasonable agreement between data of the ion-enhanced sticking of CH_3 on a-C:H and a corresponding rate equation model. Besides, it could also be plausibly derived from simple geometric considerations, assuming that surface sites are arranged hexagonally in a plane, and that directly neighboring dangling bonds can recombine. As, on the one hand, the data in [63] have considerable errors and, on the other hand, the ordered hexagonal arrangement is not a realistic picture of an amorphous hydrocarbon surface, we treat B as a free parameter in our model within the interval from 5 to 15.

The term A in process (c), the thermal desorption of oxygen, is a temperature-dependent rate constant. In its most simple form, assuming a well defined and constant desorption energy E_d, it is given by $A = n_0 \nu \exp(-E_d/k_B T)$, where ν is the vibrational frequency of the adsorbed oxygen, k_B is the Boltzmann constant and T is the surface temperature. However, in many cases the assumption of a well defined desorption energy will fail. For an amorphous material such as a-C:H it is more likely that the desorption energy depends on the actual chemical environment of the surface carbon atom. Indeed, the observed gradual increase of the erosion rate with decreasing temperature cannot be modeled assuming a fixed E_d, but an almost step-like behavior, corresponding to the rather abrupt transition from a completely empty to a completely O-covered surface, results. A simple attempt to simulate the effect of a distribution of desorption energies is to write A as a convolution of a Boltzmann factor with a Gaussian distribution centered around E_d with a width σ,

$$A = n_0 \nu \frac{1}{\sqrt{2\pi}\sigma} \int \exp\left(\frac{-E}{k_B T}\right) \exp\left(\frac{-(E - E_d)^2}{2\sigma^2}\right) \mathrm{d}E. \tag{5}$$

This treatment is not strictly appropriate, as it neglects the preferential depopulation of the sites with lower desorption energy and keeps the distribution of desorption energies constant. Its simplicity, however, allows the rate equations to be solved analytically.

The time derivatives of Θ_O and Θ_r can be read from table 1 as

$$n_0 \frac{\mathrm{d}\Theta_O}{\mathrm{d}t} = j_{O_2} p^C_{ad} \Theta_C + j_{O_2} p^r_{ad} \Theta_r - (A + j_{ion} Y_{ALACS}) \Theta_O, \tag{6}$$

$$n_0 \frac{\mathrm{d}\Theta_r}{\mathrm{d}t} = j_{ion} Y_r (1 - \Theta_O - B\Theta_r) - j_{O_2} (p^r_{ad} + p_{CS} + Y_{CE} D) \Theta_r. \tag{7}$$

In steady state the derivatives vanish, and solving equations (6) and (7) together with

$$\Theta_C + \Theta_O + \Theta_r = 1 \tag{8}$$

yields

$$\begin{aligned}
\Theta_C &= 1 - \Theta_O - \Theta_r, \\
\Theta_O &= \frac{j_{O_2}^2 + c_1 j_{O_2}}{j_{O_2}^2 + c_2 j_{O_2} + c_3}, \\
\Theta_r &= \frac{c_3}{B(j_{O_2}^2 + c_2 j_{O_2} + c_3)}
\end{aligned}$$

with

$$\begin{aligned}
c_1 &= j_{ion} Y_r \frac{(B-1)p_{ad}^C + p_{ad}^r}{z}, \\
c_2 &= c_1 + \frac{A}{p_{ad}^C} + j_{ion} Y_{ALACS} \frac{p_{CS} + Y_{CE} D}{z}, \\
c_3 &= B j_{ion} Y_r \frac{A + j_{ion} Y_{ALACS}}{z}, \\
z &= p_{ad}^C \left(p_{ad}^r + p_{CS} + Y_{CE} D\right).
\end{aligned} \tag{9}$$

5.3. Thermal yield

Some elaborate rate equation models can be found in the literature to describe the temperature-dependent yield Y_{CE} of carbon combustion [64, 65]. As CE as such is not in the focus of this paper, we take simply a fit to the experimental yield Y_{CE} from our own experiments without ion bombardment as input for the model. The fit function is,

$$Y_{CE} = Y_0 \exp\left(-E_a/(k_B T)\right), \tag{10}$$

where k_B and T are the Boltzmann constant and temperature, respectively. The fit to the rate without ion bombardment, $\Gamma_{CE} = j_{O_2} Y_{CE}$, shown as dashed line in figure 8, was obtained with $Y_0 = 1.245 \times 10^5$ and an activation energy $E_a = 1.29\,\text{eV}$, which is close to that reported by Gozzi *et al* [66] for the formation of CO at a non-oriented graphite surface of 1.2 eV. Please note that, as opposed to all other yields in this paper, Y_{CE} is a rate normalized to the O_2 flux density, not to the ion flux density.

5.4. Energy dependent quantities

The yields Y_{PS} for physical sputtering, Y_r for the ion-induced creation of reactive sites, and Y_{ALACS} for the ion-induced reaction of adsorbed oxygen all describe the action of ions and therefore depend on the ion energy and the type of ions. To derive these yields we follow the approach used earlier for the modeling of the energy dependence of chemical sputtering of a-C:H by noble gas ion bombardment in the presence of atomic hydrogen (in the following referred to as the 'hydrogen case') [37].

First of all, the PS yield is calculated using the Monte Carlo code TRIM.SP [52]. As was reported earlier [67], good agreement between measured and calculated PS yields for He^+, Ne^+

and Ar^+ bombardment of our a-C:H films was obtained assuming a carbon surface binding energy of 2.8 eV, an H/(H + C) ratio of 0.3, and a density of 2 g cm^{-3}. With these parameters the threshold energy of PS is predicted to be around 40 eV.

To explain chemical sputtering in the hydrogen case we have developed the picture that the ions break C–C bonds so that incoming atomic hydrogen can bind. By successive bond breaking and hydrogen attachment hydrocarbon molecules are formed which, after their last bond to the carbon network is broken, leave the solid. In order to calculate the bond-breaking depth profiles we have used TRIM.SP under the assumption that a minimum energy of 5 eV—a typical C–C bond strength in hydrocarbons—has to be transferred to a carbon atom to break a C–C bond. In the TRIM.SP simulation both the ion energy and the ion species (mass, nuclear charge) enter the calculation. A comparison of the experimental energy dependence and the energy dependence of the TRIM.SP depth profiles indicated that only the damage within a certain range from the surface is relevant for the chemical sputtering yield. As a step function seemed not physical, we used an exponential function to restrict the accounted bond-breaking events to a near-surface layer. Thus, the chemical sputtering yield was described by

$$Y_{\mathrm{CS}}(\text{'H case'}) = a \int_0^\infty y_{\mathrm{bb}}(x) \exp(-x/\lambda)\, \mathrm{d}x, \tag{11}$$

where a is a scaling factor of the order of 1, x is the depth below the surface, $y_{\mathrm{bb}}(x)$ is the depth-dependent bond breaking yield density in units of broken bonds per unit depth interval, and λ is the characteristic depth to which damage is accounted for. Originally, we interpreted the limitation to a near surface region as a consequence of the limited depth up to which the thermal hydrogen atoms penetrate the film [37]. The choice $\lambda = 0.4$ nm yielded good agreement and also fit well with the experimentally derived maximum penetration depth of hydrogen atoms of about 2 nm. When adapting the model to the related case of hydrogen ion bombardment [53], we found that even in this case, where the availability of hydrogen is given by the ion range distribution and, hence, not limited to near the surface, an agreement between model and experiment still required the restriction to the near surface layer. Therefore, we favored the interpretation of $\exp(-x/\lambda)$ as a depth-dependent probability of the erosion products to leave the film.

Guided by this experience, we describe the damage production Y_{r} in the Ar/O_2 case like in (11) including the exponential factor. It is reasonable to assume that the produced damage also in this case has to be close enough to the surface to enable processes (a), (e) or (f) in table 1. Regarding Y_{ALACS} it may not be necessarily a bond breaking event that is required to promote the formation of volatile carbon oxides. However, the shapes of the depth profiles for bond breaking, elastic, electronic and total energy loss, and their evolutions with energy in the relevant range are all very similar. Hence, independent of what may be the detailed mechanism behind the ion-induced reaction, we treat Y_{ALACS} also like in (11). We only allow for different scaling constants for Y_{ALACS} and Y_{r},

$$\begin{aligned} Y_{\mathrm{ALACS}} &= a_{\mathrm{ALACS}} \int_0^\infty y_{\mathrm{bb}}(x) \exp(-x/\lambda)\, \mathrm{d}x, \\ Y_{\mathrm{r}} &= a_{\mathrm{r}} \int_0^\infty y_{\mathrm{bb}}(x) \exp(-x/\lambda)\, \mathrm{d}x. \end{aligned} \tag{12}$$

It turns out that $\lambda = 2$ nm is a much better choice in the oxygen case than the 0.4 nm used for hydrogen. We have no explanation for this difference as of now.

Table 2. Model parameters, their allowed ranges, their best values, their standard deviations and their unit.

Parameter	Allowed range	Best value	Standard deviation	Unit
p_{ad}^{C}	$[0, 2]$	0.011	0.001	
p_{ad}^{r}	$[0, 2 - p_{CS}]$	1.74	0.38	
p_{CS}	$[0, 2 - p_{ad}^{r}]$	0.18	0.02	
D	$[0, \infty]$	3511	644	
a_r	$[0, \infty]$	1.1	0.2	
a_{ALACS}	$[0, \infty]$	0.41	0.01	
E_d	$[0, \infty]$	1.337	0.1[a]	eV
σ	$[0, \infty]$	0.171	0.01[a]	eV
B	$[5, 15]$	5.9		
n_0	Fixed	10^{15}		cm^{-2}
ν	Fixed	10^{13}		s^{-1}
λ	Fixed	2		nm

[a]The errors of E_d and σ were not taken from the Hessian matrix computed by the Levenberg–Marquardt algorithm, but more meaningfully from a two-dimensional scan of the parameter space.

5.5. Fitting the other parameters

Two parameters values have already been assigned: $\lambda = 2$ nm and $n_0 = 10^{15}$ cm^{-2}. As it is hardly possible to determine the adsorbed oxygen vibrational frequency ν (see (5)) independent of E_d, we choose its value within the range of typical vibrational frequencies as 10^{13} s^{-1}. Apart from these three fixed parameters there are nine more parameters in the model: p_{ad}^{C}, p_{ad}^{r}, p_{CS}, D, a_r, a_{ALACS}, E_d, σ and B. The best values and standard deviations of these nine parameters are determined by a least square fit of the model to 68 of the data points in figures 1–4 using a Levenberg–Marquardt algorithm. As neither for PS at $j_{O_2} = 0$ (six data points) nor for CE at $j_{O_2} = 0$ (seven data points) is the model sensitive to the fit parameters, the corresponding 13 additional data points are not used in the fitting procedure. The parameters, their allowed ranges, their best values and their standard deviations are listed in table 2. For completeness, the fixed parameters are also given in the table. For the oxygen adsorption probabilities p_{ad}^{C} and p_{ad}^{r} values between 0 and 2 were allowed because in the assumed adsorption process O_2 dissociates and adsorbs as two O atoms on two different sites. For p_{CS} values up to 2 were allowed because up to two carbon oxide molecules (CO in this case) could be produced per incident O_2. As p_{ad}^{r} and p_{CS} are both probabilities for processes starting from the same coverage Θ_r, and as one single oxygen atom of the O_2 molecule can only either erode or adsorb, the additional constraint $p_{ad}^{r} + p_{CS} \leqslant 2$ is introduced. Finally, B was optimized in an interval from 5 to 15 which includes the value $B = 13$ given in [63].

The fit to the 68 data points yields $\chi^2 = 185$. This slightly larger-than-desired χ^2 can partly be attributed to the fact that the data points also have uncertainties in the flux ratio and temperature at which they were measured; these uncertainties were not considered in the fitting procedure.

6. Discussion of the model

6.1. Parameter values

The values of the first nine parameters in table 2 were obtained by a fitting procedure within the given ranges. There is a strong correlation between B, which limits the coverage of reactive sites to its inverse value, and D by which Y_{CE} is enhanced on a reactive site. This correlation makes it impossible to fit both parameters independently with reasonably small errors. Therefore, all nine parameters were left free in a first optimization run, and in a second run B was kept constant at the previously determined optimum. Hence, there is no standard deviation given for B. All other eight parameters are well defined with reasonable errors. E_d and σ are also strongly correlated. Within their confidence intervals, a variation of one of the two parameters can be well compensated by the other. This leads to unrealistically small standard deviations given in the Hessian matrix computed by the Levenberg–Marquardt algorithm. Therefore, more meaningful standard deviations of E_d and σ were derived by a two dimensional scan of χ^2 over these two parameters. Still, E_d and σ are rather precisely defined by the decrease of the erosion rate in the low T region. Other parameters that show an obvious correlation are a_r, p_{ad}^r and a_{ALACS}. This correlation is expected, as a_r is a coefficient of the yield of the production of reactive sites, p_{ad}^r is the probability with which oxygen adsorbs at such a site, and the ALACS mechanism, which acts on the resulting oxygen covered sites, has a_{ALACS} as coefficient.

Regarding the obtained values, a first interesting observation is that the probability p_{ad}^r for oxygen adsorption on a reactive site is much larger than the probability p_{ad}^C of adsorption on an undisturbed C site. This seems intuitively plausible. The value of $p_{ad}^r = 1.813$ means that almost every O_2 hitting a reactive site sticks there. The value of p_{ad}^C, on the other hand, is close to zero. However, the fact that it is not equal to zero has an important impact on the model at very high oxygen fluxes as will be shown later. In comparison with p_{ad}^r, the probability p_{CS} for incoming oxygen to directly lead to erosion at a reactive site is very much smaller with a value of 0.18. The high value of D means that reactive sites are about 3500 times more reactive to O_2 for CE at elevated temperatures than undisturbed C sites. The scaling parameters a_r and a_C are both of the order of 1. As $y_{bb}(x)$ in (12) is an absolute number of bond breaking events per projectile and unit depth interval, and as furthermore the integral over the exponential factor is of the order of the thickness of the interaction layer, $\int_0^\infty \exp(-x/\lambda)\,dx = \lambda = 2\,\text{nm}$, the integral is expected to give the correct order of the number of bond breaking or ion-induced reaction events in the interaction layer. Therefore, a_r and a_C are indeed expected to be of the order of 1. The mean oxygen desorption energy has a reasonable value of 1.337 eV and it's distribution a standard deviation of $\approx$10 %. It should be kept in mind, however, that as the way we treat distributed desorption energies is not strictly correct (see section 5.2), the actual values may be slightly different. Finally, $B = 5.9$ is about half the value from [63] of $B = 13$.

6.2. Energy dependence

Figure 7 shows the energy dependence of the erosion yield at 150, 300 and 800 K. The data are those presented in figure 2 and the lines are the model results. The model is in excellent agreement with all data shown. The dominant mechanisms in the model are different at the three temperatures in the figure; while at 150 K ALACS plays the dominant role, it is CS via reaction of oxygen at reactive sites at 300 K and IECE at 800 K. For both the CS and IECE mechanisms

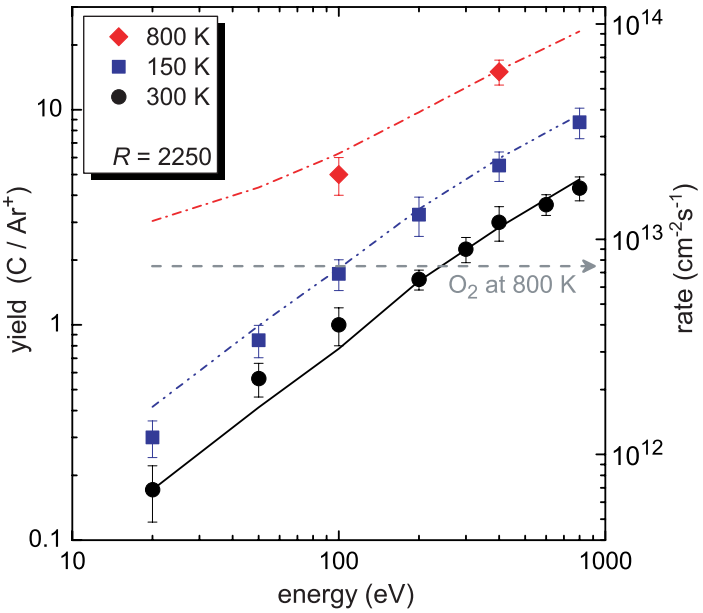

Figure 7. Comparison of the calculated erosion rates/yields as a function of ion energy (lines) with the data (symbols). The data are those shown in figure 2. The dashed line shows the measured CE yield at 800 K in the absence of ion bombardment. The flux densities are $j_{\text{ion}} = 4 \times 10^{12}\,\text{cm}^{-2}\,\text{s}^{-1}$ and $j_{\text{O}_2} = 9 \times 10^{15}\,\text{cm}^{-2}\,\text{s}^{-1}$.

the production of reactive sites is the energy-dependent process involved, described by the yield Y_{r}. For the ALACS mechanism there are two relevant energy-dependent processes. The first is also in this case the creation of reactive sites, for it drives the build-up of an oxygen surface coverage. The second is the ion-induced reaction of adsorbed oxygen with the yield Y_{ALACS}. At 800 K the rate of the CE mechanism represents the lower limit of the erosion rate for zero ion energy or absence of ion bombardment (dashed line in figure 7).

6.3. Temperature dependence

The lower half of figure 8 shows the temperature dependence of the erosion rate without ion bombardment and for ion energies between 20 and 800 eV. In the case without ions the line is simply a fit to the data by (10) which was used as a model input for Y_{CE}. All other lines are the model results. The model captures the prominent features of the temperature dependence and the overall agreement between model and data is good.

The upper half of figure 8 shows the corresponding behavior of the coverages. Below 400 K Θ_{O} increases because the thermal oxygen desorption becomes less effective. Below about 200 K Θ_{O} even becomes the largest of the coverages. Accordingly, in this temperature range ALACS dominates the erosion rate. The model includes both adsorption of O_2 at undisturbed carbon sites and on reactive sites. The fit of the model to the data gives a very much higher probability for the adsorption of O_2 on reactive sites. Thus, the dominant process cycle at very low temperature is the creation of reactive sites ((b) in table 1) followed by the adsorption of oxygen (a) and ALACS (d) as final erosion step. Although adsorbing on a reactive site, the model assumes

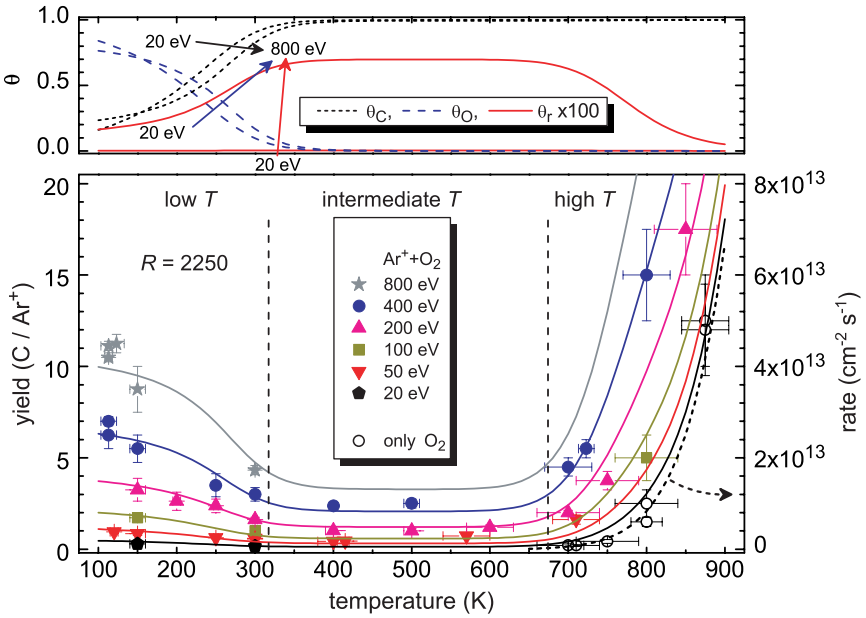

Figure 8. Lower panel: comparison of the calculated erosion rates/yields (solid lines) as a function of target temperature with the data (symbols). The dashed line is an exponential fit to the CE rate (open circles). The data are those shown in figure 3. Upper panel: coverages Θ_C, Θ_O and Θ_r as a function of temperature at two different ion energies of 20 and 800 eV. The flux densities are $j_{ion} = 4 \times 10^{12}\,\mathrm{cm}^{-2}\,\mathrm{s}^{-1}$ and $j_{O_2} = 9 \times 10^{15}\,\mathrm{cm}^{-2}\,\mathrm{s}^{-1}$.

that O_2 adsorbs into a weakly bound state with a desorption energy of 1.34 ± 0.17 eV in order to explain the decrease of the erosion rate with increasing T. The rise of Θ_O toward very low temperatures decreases Θ_C and hence there are less undisturbed C sites on which new reactive sites could be created. Therefore, also Θ_r decreases.

In the intermediate temperature range the oxygen surface coverage has become almost zero due to the increased thermal desorption of adsorbed oxygen and CE is not yet effective. The dominant erosion mechanism is the CS mechanism and it maintains the erosion rate on a comparatively low level. Erosion is driven by the cycle of the creation of reactive sites by ion impact and the direct erosion reaction of O_2 at these sites. Oxygen adsorption at reactive sites followed by its thermal desorption is an additional loss mechanism of reactive sites and hence competes with erosion.

At temperatures beyond 650 K thermal chemical erosion enhanced by ion bombardment (CE + IECE) takes over the leading role. The rates of the CS and IECE mechanisms are both proportional to Θ_r. This coverage is rather constant over most of the temperature range but decreases gradually toward very low and very high temperatures. On the high-temperature side the extremely high reactivity of oxygen at reactive sites lets IECE become a very effective loss mechanism of reactive sites, thus self-limiting its rate.

6.4. Flux dependence

As can be seen from (9), the erosion rate depends explicitly on both particle flux densities j_{ion} and j_{O_2} and not only on their ratio. This is a consequence of the thermal oxygen desorption.

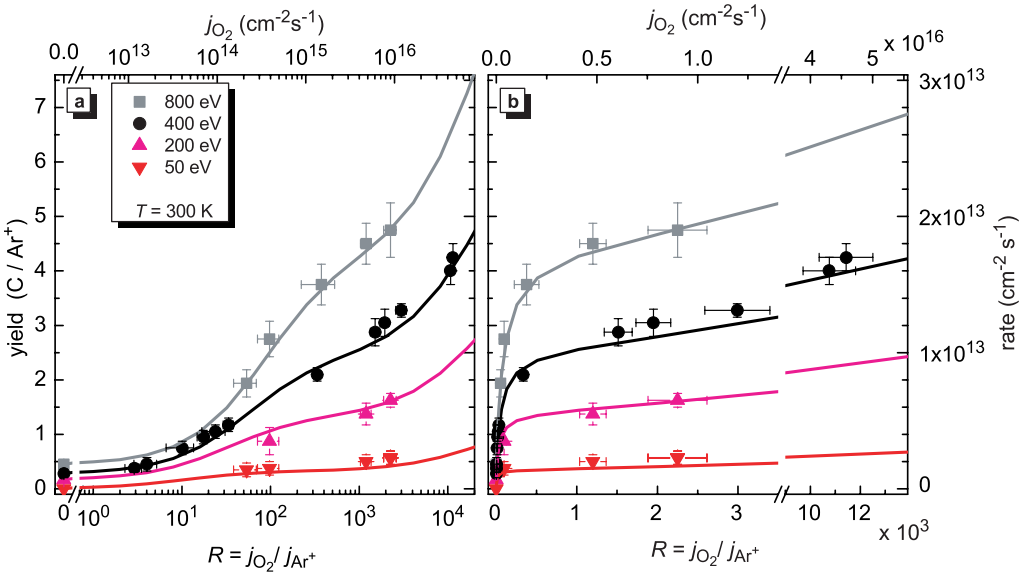

Figure 9. Comparison of the calculated erosion rates/yields (solid lines) as a function of the oxygen-to-ion flux ratio at 300 K with the data (symbols). The data are those shown in figure 1. (a) Shows the data on a logarithmic abscissa on the right-hand side of the axis break and (b) shows a linear representation.

The vibrational frequency ν in the desorption rate (5) introduces an additional time scale into the model beside the time scale given by the particle fluxes. Despite this fact we stay with the presentation of the data as a function of the O_2-to-ion flux ratio because this quantity conveys how much more oxygen reaches the surface than ions. The reader should, however, keep in mind that the ion flux density is held constant for all experiments and only the O_2 flux density is varied.

Figure 9 shows a comparison of the experimental and modeled dependences on the O_2-to-ion flux ratio at room temperature for four different ion energies as in figure 1. The general agreement is good. The model lines show two inflection points which are not evident in the data but do not contradict the data either. The origin of these inflection points can be seen from the contributions of the individual erosion mechanisms, plotted as dashed and dotted lines in figure 10. The erosion rate is the sum of the rates of the CS and ALACS mechanisms plus the constant PS rate. As the temperatures are too low, CE and IECE do not contribute. The CS rate has a maximum around $R = 1000$ while the ALACS rate increases monotonically and dominates above $R \approx 5000$. At these high oxygen fluxes the oxygen coverage becomes bigger than 10% even at room temperature and—although p_{ad}^{C} is small compared with p_{ad}^{r}—oxygen adsorption happens mostly on undisturbed carbon sites because high oxygen fluxes keep Θ_r small. At 110 K, due to reduced thermal oxygen desorption the oxygen coverage becomes much higher and exceeds 50% already at $R \approx 200$. At very high flux ratios above $R \approx 10^6$ (not shown in figure 1) the erosion yield saturates at the value Y_{ALACS}.

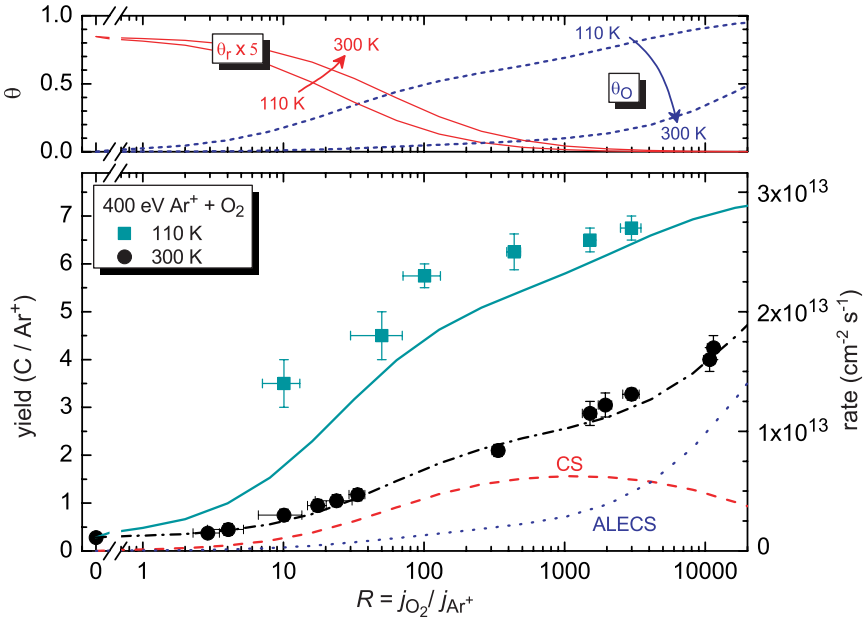

Figure 10. Lower panel: comparison of the calculated erosion rates/yields (lines) as a function of the oxygen-to-ion flux ratio at two different target temperatures with the corresponding data (symbols). The data are those shown in figure 4. Upper panel: the corresponding surface coverages Θ_O and Θ_r. The ion energy and flux density were 400 eV and 4×10^{12} cm^{-2} s^{-1}, respectively.

7. Summary and conclusions

Our experiments provide a direct proof of the synergistic erosion of a-C:H films with energetic species—in our case Ar^+ ions—and thermal molecular oxygen. Such a synergism had been previously postulated based on investigations of the erosion of polymers [39] and hard a-C:H [23] in oxygen plasmas and explicitly shown as a function of temperature by Ar^+ ion bombardment of graphite [46]. Very recently, Raballand *et al* [12] exposed spores of *Bacillus atrophaeus* and *Aspergillus niger* to Ar^+ bombardment and molecular oxygen and found a high-inactivation efficiency due to synergistic erosion of the spores.

When bombarded by an Ar^+ ion beam an a-C:H film is physically sputtered if the ion energy exceeds about 40 eV. When additionally thermal molecular oxygen reaches the surface the erosion rates increase rapidly with the oxygen flux density. At an oxygen-to-ion flux ratio of ≈10 000, room temperature and 400 eV ion energy an erosion yield of ≈4 C atoms per incident ion is found. The yield increases with ion energy, indicating that kinematic processes are important in the underlying mechanism. The yield also increases with temperature from about 700 K onwards, the temperature at which thermal chemical erosion (combustion) sets in even without ion bombardment. Moreover, the additional ion bombardment increases the erosion rate also in this temperature range. The erosion rates at high temperatures are systematically higher than the sum of the synergistic erosion rates at room temperature and the thermal chemical erosion rate at the respective temperature. This finding indicates that there is an additional mechanism active, which we explain as an increased reactivity of the surface toward O_2 due to ion-induced damage. Decreasing the temperature below room temperature the yield increases again down to the lowest

investigated temperature of 110 K. This notable behavior is explained in terms of an ion-induced reaction of weakly adsorbed oxygen species; as temperature rises, the rate of desorption of these adsorbed species increases and the surface's oxygen coverage decreases.

A rate equation model was developed which accounts for three surfaces coverages, undisturbed carbon sites, oxygen covered sites and reactive sites. Several processes transform the coverages into each other. These are, besides the erosion processes themselves, adsorption of oxygen on either undisturbed or reactive sites, thermal desorption of oxygen and the ion-induced creation of reactive sites.

We consider five erosion processes: physical sputtering (PS), chemical sputtering by direct reaction of incoming O_2 at active sites (CS), chemical sputtering by the ion-induced reaction of adsorbed oxygen (ALACS), thermal chemical erosion (CE) and an ion-induced enhancement of thermal chemical erosion (IECE). All energy-dependent processes are described based on TRIM.SP calculations. The only exception is thermal chemical erosion, which is not modeled based on a microscopic picture. Instead, the temperature-dependent yield per O_2 molecule determined in experiments without ion bombardment is used as an input for the model.

The model captures all basic features of the investigated dependences and leads to generally good agreement with the data. Thus, the good agreement between data and model shows that our microscopic picture of the underlying erosion mechanisms can indeed explain the observed dependences. This is what the model is intended for. Nevertheless, this agreement does not provide a proof that the mechanisms are really the ones assumed in the model. In order to validate the assumed mechanisms, more data besides erosion rates are required. As the model also predicts surface coverages, the measurement of the oxygen surface coverage during particle bombardment would be specifically desirable.

It is an obvious remaining question to which extent the synergism between O_2 and ions contributes to erosion in typical oxygen plasma applications. As was mentioned in the introduction, it was in fact already concluded from plasma experiments that the contribution of this synergistic interaction is large [23, 39].

Formally, the model is able to predict erosion yields of a-C:H films exposed to thermal molecular oxygen and ion bombardment for any (chemically inert) ion species, ion-energy, ion and oxygen flux density and temperature below 875 K. In an oxygen plasma the ions are also reactive and contribute to chemical sputtering by reaction at the end of their range. However, if this latter process is sufficiently independent of all other erosion mechanisms we can still estimate the contribution of the synergism between O_2 and ions with our model. We do this for a low temperature plasma experiment for which all the model's required input parameters are known.

For an oxygen ion flux density of $1.2 \times 10^{16}\,\mathrm{cm^{-2}\,s^{-1}}$, the vast majority of which was carried by O_2^+, a molecular oxygen flux density of $6.7 \times 10^{17}\,\mathrm{cm^{-2}\,s^{-1}}$, a temperature of 300 K of the hard a-C:H sample, and an ion energy of 260 eV, Landkammer [23] measured an erosion rate of $2.3 \times 10^{16}\,\mathrm{cm^{-2}\,s^{-1}}$. As TRIM.SP cannot treat molecular ions, we treat the O_2^+ ions as O^+ ions at doubled flux density and half energy. Our model then predicts a total erosion rate of $\Gamma_{\mathrm{tot}} = 2.5 \times 10^{16}\,\mathrm{cm^{-2}\,s^{-1}}$ in close agreement with the experimental value. The contributions of the individual processes are $\Gamma_{\mathrm{phys}} = 2.6 \times 10^{15}\,\mathrm{cm^{-2}\,s^{-1}}$, $\Gamma_{\mathrm{CS}} = 1.9 \times 10^{15}\,\mathrm{cm^{-2}\,s^{-1}}$, $\Gamma_{\mathrm{ALACS}} = 2.02 \times 10^{16}\,\mathrm{cm^{-2}\,s^{-1}}$ and $\Gamma_{\mathrm{CE}} = \Gamma_{\mathrm{IECE}} = 0$. However, the model does not include the ions' own contribution to chemical sputtering. If every oxygen in the ion contributed to the formation of CO_2 or CO the resulting erosion rate would be $1.2 \times 10^{16}\,\mathrm{cm^{-2}\,s^{-1}}$ or $2.4 \times 10^{16}\,\mathrm{cm^{-2}\,s^{-1}}$, respectively. Thus, our estimated rate of synergistic erosion as well as the

maximum possible contribution of chemical reactions of the oxygen ions can both explain the experimental result.

Despite this successful application of the model to parameters of a plasma experiment it should be kept in mind that the values of the model's nine free parameters are the result of a fit to 68 data points only in a limited parameter range. To test or improve the model a comparison with or adjustment to experimental data in an extended parameter range is required. In all experiments presented here the ion flux density was never varied. However, the modeled rate depends explicitly on both flux densities, not only on their ratio. For example, the model predicts that when increasing both flux densities while keeping their ratio j_{O_2}/j_{ion} constant the temperature below which the ALACS mechanism leads to enhanced erosion should also increase. Experiments at extremely high O_2-to-ion flux ratios where the erosion rate is in saturation should yield values for Y_{ALACS}; the model predicts saturation at a total erosion yield of $Y_{PS} + Y_{ALACS}$ if the temperature is low enough so that Y_{CE} is negligible. In the other extreme, at O_2-to-ion flux ratios around unity but sufficiently high ion flux densities so that the obtained rates are easily detectible, the CS probability on a maximally activated surface, $p_{CS}\Theta_r^{max}$, could be determined with reasonably small error.

References

[1] Hartney M A, Hess D W and Soane D S 1989 Oxygen plasma etching for resist stripping and multilayer lithography *J. Vac. Sci. Technol.* B **7** 1

[2] Massi M, Mansano R D, Maciel H S, Otani C, Verdonck P and Nishioka L N B M 1999 Effects of plasma etching on DLC films *Thin Solid Films* **343–344** 381

[3] Urruchi W I, Massi M, Maciel H S, Otani C and Nishioka L N 2000 Etching of DLC films using a low intensity oxygen plasma jet *Diamond Relat. Mater.* **9** 685

[4] Steudel S, Myny K, De Vusser S, Genoe J and Heremans P 2006 Patterning of organic thin film transistors by oxygen plasma etch *Appl. Phys. Lett.* **89** 183503

[5] Liu C-C, Nealey P F, Ting Y-H and Wendt A E 2007 Pattern transfer using poly(styrene-block-methyl methacrylate) copolymer films and reactive ion etching *J. Vac. Sci. Technol.* B **25** 1963

[6] Meng E, Li P-Y and Tai Y-C 2008 Plasma removal of parylene C *J. Micromech. Microeng.* **18** 045004

[7] Hirakuri K K, Kuwashima K, Tatsuta K and Sato K 2005 Etching of diamond-like carbon films deposited on polyethylene terephtalate *Diamond Relat. Mater.* **14** 1067

[8] Eggenstein F, Senf F, Zeschke T and Gudat W 2001 Cleaning of contaminated XUV-optics at BESSY II *Nucl. Instrum. Methods* A **467** 325

[9] Rossi F, Kylián O and Hasiwa M 2006 Decontamination of surfaces by low pressure plasma discharges *Plasma Process. Polym.* **3** 431

[10] Moisan M, Berbeau J, Crevier M-C, Pelletier J, Philip N and Saoudi B 2002 Plasma sterilization. Methods and mechanisms *Pure Appl. Chem.* **74** 349

[11] Lerouge S, Wertheimer M R and Yahia L'H 2001 Plasma sterilization: a review of parameters, mechanisms, and limitations *Plasmas Polym.* **6** 175

[12] Raballand V, Benedikt J, Wunderlich J and von Keudell A 2008 Inactivation of *Bacillus atrophaeus* and of *Aspergillus niger* using beams of argon ions, of oxygen molecules and of oxygen atoms *J. Phys. D: Appl. Phys.* **41** 115207

[13] Federici G *et al* 2001 Plasma–material interactions in current tokamaks and their implications for next step fusion devices *Nucl. Fusion* **41** 1967

[14] Jacob W 2005 Redeposition of hydrocarbon layers in fusion devices *J. Nucl. Mater.* **337–339** 839

[15] von Keudell A, Hopf C, Schwarz-Selinger T and Jacob W 1999 Surface loss probabilities of hydrocarbon radicals on amorphous hydrogenated carbon film surfaces: consequences for the formation of re-deposited layers in fusion experiments *Nucl. Fusion* **39** 1451
[16] Counsell G *et al* 2006 Tritium retention in next step devices and the requirements for mitigation and removal techniques *Plasma Phys. Control. Fusion* **48** 189
[17] Hsu W L 1989 Glow discharge removal of codeposited carbon films in graphite-lined tokamak reactors. *J. Vac. Sci. Technol.* A **7** 1047
[18] Jacob W, Landkammer B and Wu C H 1999 Removal of codeposited layers by ECR discharge cleaning *J. Nucl. Mater.* **266–269** 552
[19] Mueller D, Blanchard W, Collins J, Hosea J, Kamperschroer J, LaMarche P H, Nagy A, Owens D K and Skinner C H 1997 Tritium removal from TFTR *J. Nucl. Mater.* **241–243** 897
[20] Moormann R, Alberici S, Hinssen H-K and Wu C H 2000 Examination of codeposited a-C:D layers in oxygen *Fusion Eng. Des.* **49–50** 295
[21] Hopf C, Rohde V, Jacob W, Herrmann A, Neu R, Roth J and ASDEX Upgrade Team 2007 Oxygen glow discharge cleaning in ASDEX Upgrade *J. Nucl. Mater.* **363–365** 882
[22] Marsh H and Kuo K 1989 Kinetics and catalysis of carbon gasification *Introduction to Carbon Science* (London: Butterworths) p 107
[23] Landkammer B 1999 Untersuchung der Erosion von Kohlenwasserstoffschichten in Sauerstoff-Gasentladungen *PhD Thesis* Universität Bayreuth
[24] Stanmore B R, Brilhac J F and Gilot P 2001 The oxidation of soot: a review of experiments, mechanisms and models *Carbon* **39** 2247
[25] Müller J-O, Su D S, Jentoft R E, Kröhnert J, Jentoft F C and Schlögl R 2005 Morphology-controlled reactivity of carbonaceous materials towards oxidation *Catal. Today* **102** 259
[26] Balden M, Klages K U, Jacob W and Roth J 2005 Oxidative erosion of graphite in air between 600 and 1000 K *J. Nucl. Mater.* **341** 31
[27] Wang W, Jacob W and Roth J 1997 Oxidation and hydrogen isotope exchange in amorphous, deuterated carbon films *J. Nucl. Mater.* **245** 66
[28] Rosner D E and Allendorf H D 1970 *Proc. Int. Conf. in Metallurgy and Materials Science (Philadelphia, 8–10 September 1969)* ed G R Belton and W L Worrell (New York: Plenum) pp 231–51
[29] Cataldo F 2007 Ozone reaction with carbon nanostructures 2: the reaction of ozone with milled graphite and different carbon black grades *J. Nanosci. Nanotechnol.* **7** 1446
[30] Hechtl E, Bohdansky J and Roth J 1981 The sputtering yield of typical impurity ions for different fusion reactor materials *J. Nucl. Mater.* **103–104** 333
[31] Hechtl E and Bohdansky J 1984 Sputtering behavior of graphite and molybdenum at low bombarding energies *J. Nucl. Mater.* **122–123** 1431
[32] Refke A, Philipps V, Vietzke E, Erdweg M and von Seggern J 1994 Interaction of energetic oxygen with different boron/carbon materials. *J. Nucl. Mater.* **212–215** 1255
[33] Jacob W and Roth J 2007 Chemical sputtering *Sputtering by Particle Bombardment IV* (*Topics in Applied Physics* vol 110) ed R Behrisch and W Eckstein (Berlin: Springer) pp 329–400
[34] Coburn J W and Winters H F 1979 Ion- and electron-assisted gas–surface chemistry—an important effect in plasma etching *J. Appl. Phys.* **50** 3189
[35] Vietzke E, Flaskamp K and Philipps V 1982 Hydrocarbon formation in the reaction of atomic hydrogen with pyrolytic graphite and the synergistic effect of argon ion bombardment *J. Nucl. Mater.* **111–112** 763–8
[36] Hopf C, von Keudell A and Jacob W 2002 Chemical sputtering of hydrocarbon films by low-energy Ar^+ ion and H atom impact *Nucl. Fusion* **42** L27
[37] Hopf C, von Keudell A and Jacob W 2003 Chemical sputtering of hydrocarbon films *J. Appl. Phys.* **94** 2373
[38] Landkammer B, von Keudell A and Jacob W 1999 Erosion of thin hydrogenated carbon films in oxygen, oxygen/hydrogen and water plasmas *J. Nucl. Mater.* **264** 48

[39] Baggerman J A G, Visser R J and Collart J H 1994 Ion-induced etching of organic polymers in argon and oxygen radio-frequency plasmas *J. Appl. Phys.* **75** 758
[40] Gokan H and Esho S 1984 Sputtering yield of carbon atoms in organic materials for oxygen bombardment. *J. Electrochem. Soc.* **131** 1105
[41] Murillo R, Poncin-Epaillard F and Segui Y 2007 Plasma etching of organic material: combined effects of charged and neutral species *Eur. Phys. J. Appl. Phys.* **37** 299
[42] Hopf C, Jacob W and Rohde V 2008 Oxygen glow discharge cleaning in nuclear fusion devices *J. Nucl. Mater.* **374** 413
[43] Ferreira J A, Tabarés F L and Tafalla D 2007 Removal of carbon deposits in narrow gaps by oxygen plasmas at low pressure *J. Vac. Sci. Technol.* A **25** 746
[44] Schwarz-Selinger T, Genoese F, Hopf C and Jacob W 2008 Carbon removal from tile-gap structures with oxygen glow discharges *J. Nucl. Mater.* at press
[45] Collart E J H, Baggerman J A G and Visser R J 1995 On the role of atomic oxygen in the etching of organic polymers in a radio-frequency oxygen discharge *J. Appl. Phys.* **78** 47
[46] Vietzke E, Tanabe T, Philipps V, Erdweg M and Flaskamp K 1987 The reaction of energetic O_2^+, thermal O_2, and thermal O_2/Ar^+ on graphite and the use of graphite for oxygen collector probes *J. Nucl. Mater.* **145–147** 425
[47] Hopf C, Schlüter M and Jacob W 2007 Chemical sputtering of carbon films by argon ions and molecular oxygen at cryogenic temperatures *Appl. Phys. Lett.* **90** 224106
[48] Maya P N, von Toussaint U and Hopf C 2008 Synergistic erosion process of hydrocarbon films: a molecular dynamics study *New J. Phys.* **10** 023002
[49] Jacob W, Hopf C, von Keudell A, Meier M and Schwarz-Selinger T 2003 Particle-beam experiment to study heterogeneous surface reactions relevant to plasma-assisted thin film growth and etching *Rev. Sci. Instrum.* **74** 5123
[50] Schwarz-Selinger T, von Keudell A and Jacob W 1999 Plasma chemical vapor deposition of hydrocarbon films: the influence of hydrocarbon source gas on the film properties *J. Appl. Phys.* **86** 3988
[51] Hopf C, Schlüter M and Jacob W 2008 Chemical sputtering of a-C:H films by simultaneous exposure to energetic Ar^+ ions and water vapor *J. Phys.: Conf. Series* **100** 062012
[52] Eckstein W 1991 *Computer Simulation of Ion–Solid Interactions* (*Springer Series in Materials Science*) 1st edn (Berlin: Springer)
[53] Hopf C and Jacob W 2005 Bombardment of graphite with hydrogen isotopes: a model for the energy dependence of the chemical sputtering yield *J. Nucl. Mater.* **342** 141
[54] Roth J and García-Rosales C 1996 Analytic description of the chemical erosion of graphite by hydrogen ions *Nucl. Fusion* **36** 1647
Roth J and García-Rosales C 1997 Analytic description of the chemical erosion of graphite by hydrogen ions *Nucl. Fusion* **37** 897 (corrigendum)
[55] Schlüter M, Hopf C, Schwarz-Selinger T and Jacob W 2008 Temperature dependence of the chemical sputtering of amorphous hydrogenated carbon films by hydrogen *J. Nucl. Mater.* **376** 33
[56] Mullins C B and Coburn J W 1994 Ion-beam-assisted etching of Si with fluorine at low temperatures *J. Appl. Phys.* **76** 7562
[57] Vugts M J M, Hermans L J F and Beijerinck H C W 1996 Ion-assisted Si/XeF_2 etching: temperature dependence in the range 100–1000 K *J. Vac. Sci. Technol.* A **14** 2820
[58] Sebel P G M, Hermans L J F and Beijerinck H C W 2000 Reaction layer dynamics in ion-assisted Si/XeF_2 etching: temperature dependence *J. Vac. Sci. Technol.* A **18** 2759
[59] Vugts M J M, Verschueren G L J, Eurlings M F A, Hermans L J F and Beijerinck H C W 1996 Si/XeF_2 etching: temperature dependence *J. Vac. Sci. Technol.* A **14** 2766
[60] Joubert O, Pelletier J and Arnal Y 1989 The etching of polymers in oxygen-based plasmas: a parametric study *J. Appl. Phys.* **65** 5096

[61] Vanderlinde W E and Ruoff A L 1988 Reactive ion beam etching of polyimide thin films *J. Vac. Sci. Technol.* B **6** 1621
[62] Standaert T E F M, Matsuo P J, Li X, Oehrlein G S, Lu T-M, Gutmann R, Rosenmayer C T, Bartz J W, Langan J G and Entley W R 2001 High-density plasma patterning of low dielectric constant polymers: a comparison between polytetrafluorethylene, parylene-N, and poly(arylene ether) *J. Vac. Sci. Technol.* A **19** 435
[63] Hopf C, Jacob W and von Keudell A 2005 Ion-induced surface activation, chemical sputtering, and hydrogen release during plasma-assisted hydrocarbon film growth *J. Appl. Phys.* **97** 094904
[64] Haynes B S 2001 A turnover model for carbon reactivity. I. Development *Combust. Flame* **126** 1421
[65] Makino A, Namikiri T and Kimura K 2003 Combustion rates of graphite rods in the forward stagnation field with high-temperature airflow *Combust. Flame* **132** 743
[66] Gozzi D, Guzzardi G and Salleo A 1996 High temperature reactivity of different forms of carbon at low oxygen fugacity *Solid State Ion.* **83** 177
[67] Jacob W, Hopf C and Schlüter M 2006 Chemical sputtering of carbon materials due to combined bombardment by ions and atomic hydrogen *Phys. Scr.* T **124** 32